Supporting Information

Supplementary Figures

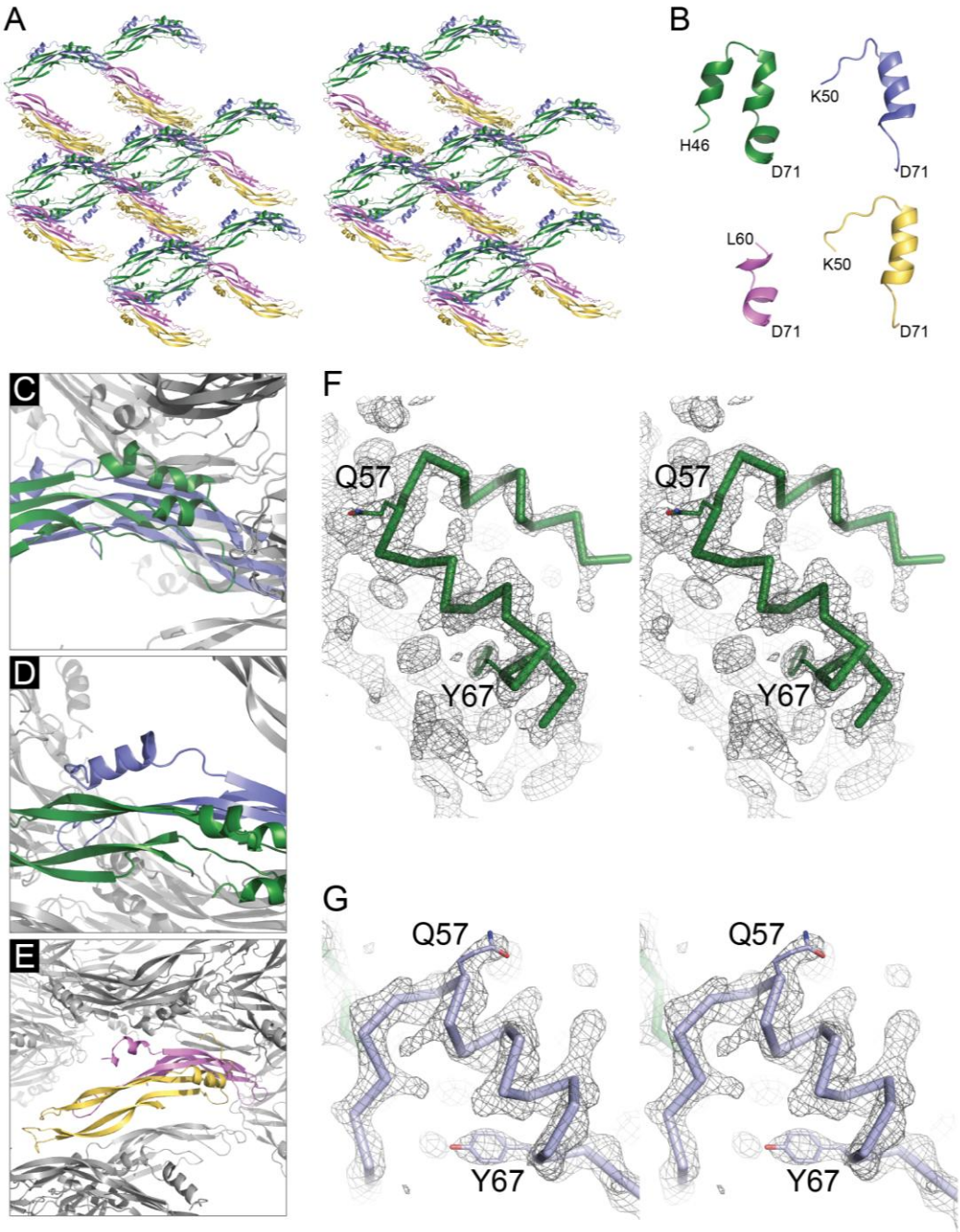

Supplementary Figure S1. Crystal packing of PRDC and different conformations of the N-terminus. (**A**) Stereo view of PRDC depicting an overview of the crystal packing within multiple asymmetric units. Two PRDC dimers (Chain A and B, colored green and blue; Chain C and D, colored purple and yellow) generate each asymmetric unit. (**B**) Differences in the organization and structure of the helix at the N-terminus for the four chains. (**C**) Zoomed in view of Chain A showing its N-terminal packing interactions with the neighboring ASU. (**D-E**) Zoomed in view of Chain B (D) and Chains C and D (E) showing their N-terminus is unaffected by crystal packing interactions as they are seen stretching out into the nearby solvent channels. (**F-G**) Stereo view of the electron density and corresponding backbone ribbon diagram for the N-terminal helices of Chain A (F) and Chain B (G). The SIGMAA weighted electron density maps ($2F_o$-F_c) are shown at a contour of 1σ.

A

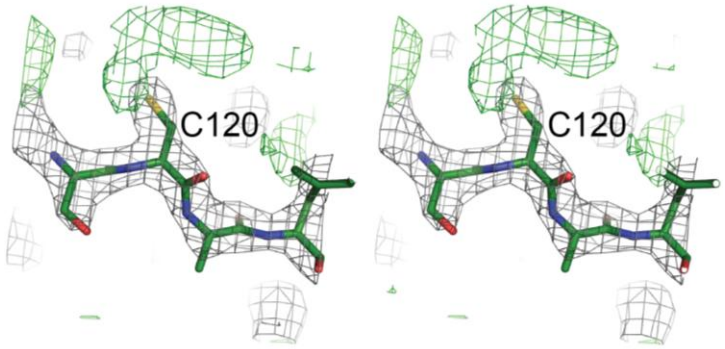

B

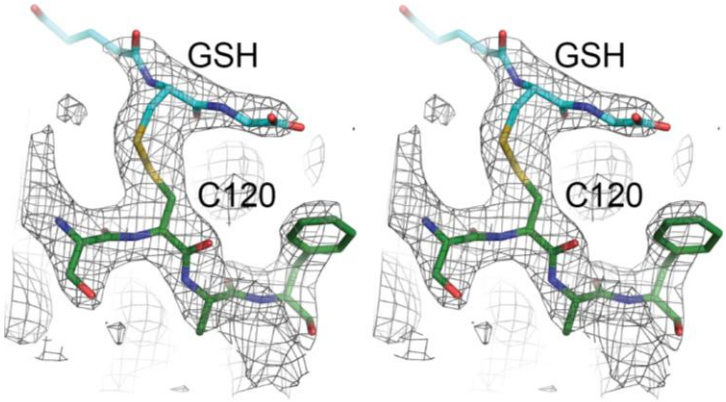

Supplementary Figure S2. Covalent modification of C120S by glutathione. (**A**) Stereoview showing the extra electron density near C120 as indicated by the positive (green) density in the F_o-F_c difference map. $2F_o$-F_c is shown in the black density and the extra C120 density becomes apparent below 0.7σ (**B**) Stereoview of the same location as in (A) glutathione modeled and covalently linked to C120. The SIGMAA weighted electron density maps ($2F_o$-F_c) are shown at a contour of 1σ.

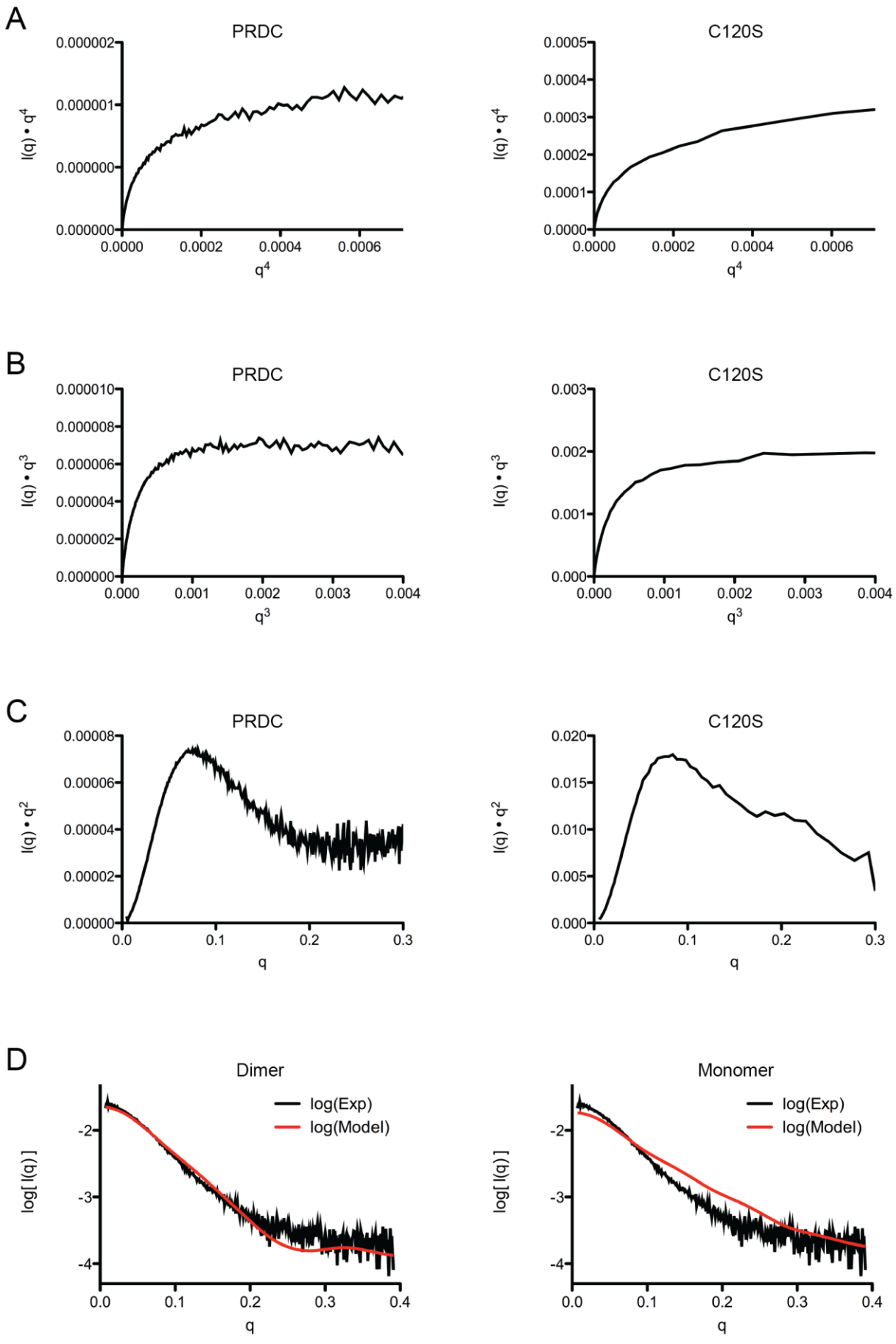
A
PRDC
C120S
I(q) • q^4
q^4
B
PRDC
C120S
I(q) • q^3
q^3
C
PRDC
C120S
I(q) • q^2
q
D
Dimer
Monomer
log(Exp)
log(Model)
log[I(q)]
q

Supplementary Figure S3. SAXS analysis of PRDC. (**A-B**) Porod plots of PRDC and PRDC^{C120S} data at 1.0 and 0.6 mg/ml respectively. $I(q)\bullet q^4$ versus q^4 plots of the samples indicates that the protein samples exhibit significant flexibility as a steady plateau is not reached (A) whereas a plateau is stably reached in the $I(q)\bullet q^3$ versus q^3 representation (B). Together, this indicates that the protein sample maintains a globular fold with inherent flexibility. (**C**) Kratky plots of PRDC and PRDC^{C120S} at the same concentrations showing a defined peak within the low q range with increasing intensity in the high q range, recapitulating the results from the Porod analysis. (**D**) FoXS scattering profiles obtained from the PRDC crystal structure compared to the PRDC solution scattering data at 1.0 mg/ml. A more significant fit to the solution scattering data is obtained for the theoretical dimer profile (Chains A and B, χ score of 0.69) as compared to the theoretical monomer profile (Chain B, χ score of 2.01).

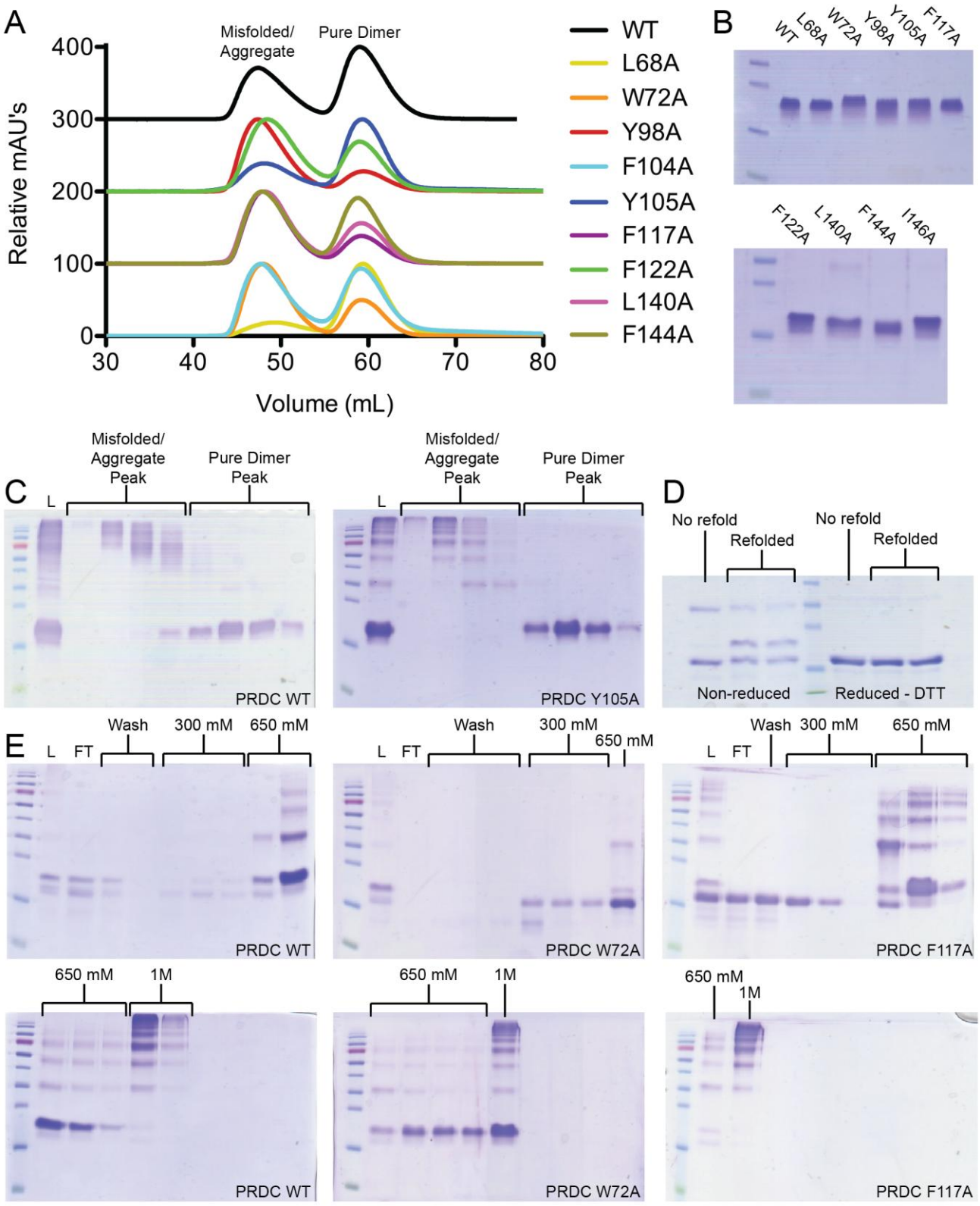
A
Misfolded/
Aggregate
Pure Dimer
Relative mAU's
400
300
200
100
0
30
40
50
60
70
80
Volume (mL)
WT
L68A
W72A
Y98A
F104A
Y105A
F117A
F122A
L140A
F144A
B
WT
L68A
W72A
Y98A
Y105A
F117A
F122A
L140A
F144A
I146A
C
Misfolded/
Aggregate
Peak
Pure Dimer
Peak
L
PRDC WT
PRDC Y105A
D
No refold
Refolded
Non-reduced
Reduced - DTT
E
L
FT
Wash
300 mM
650 mM
1M
PRDC WT
PRDC W72A
PRDC F117A

Supplementary Figure S4. Production and purification of PRDC mutants. (**A**) S75 FPLC sensorgrams (scaled) showing similar elution profiles for WT and mutant PRDC proteins. Aggregate material can be found in the left peak and pure dimer material within the right peak. (**B-E**). SDS-PAGE gels showing purified WT and mutant proteins (B), S75 elution profiles of select variants (C), WT PRDC under both reducing and non-reducing (DTT) conditions immediately after refolding, indicating the oxidative shift seen for properly folded and dimeric material (D), and select heparin elution profiles for specific PRDC mutants, showing that PRDC exhibits strong heparin affinity and that the mutants maintain this heparin affinity when properly folded (E). Misfolded material either does not bind the heparin column or elutes prior to correctly folded material.

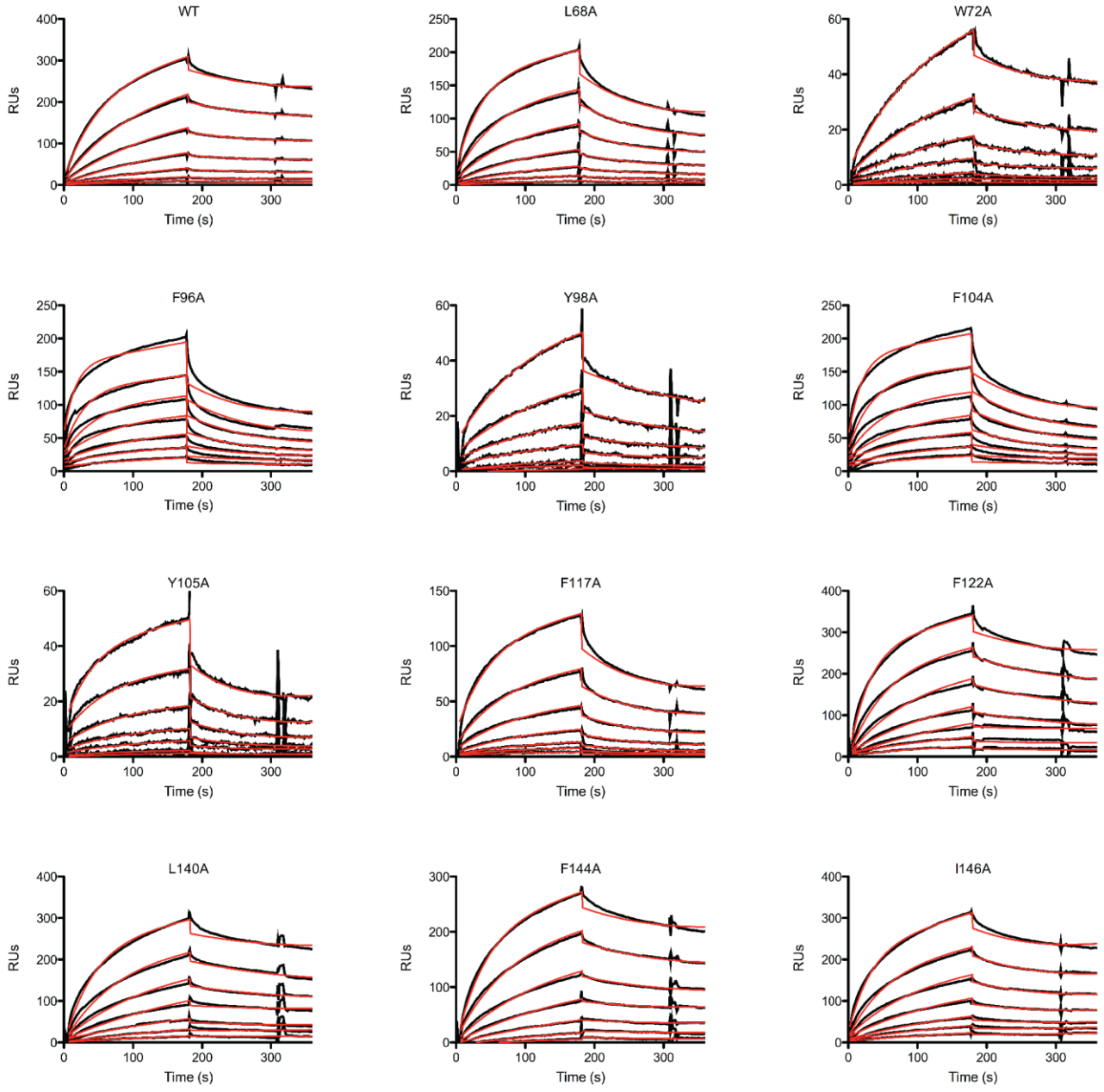
WT
L68A
W72A
F96A
Y98A
F104A
Y105A
F117A
F122A
L140A
F144A
I146A
RUs
Time (s)

Supplementary Figure S5. SPR analysis of PRDC WT and mutant binding to BMP2. SPR sensorgrams for WT and mutant PRDC binding to immobilized BMP2. Traces show raw data (black) and the fits (red) used to obtain values for k_{on} and k_{off}. PRDC was tested at concentrations ranging from 500nM (top) to 0.49nM (bottom).

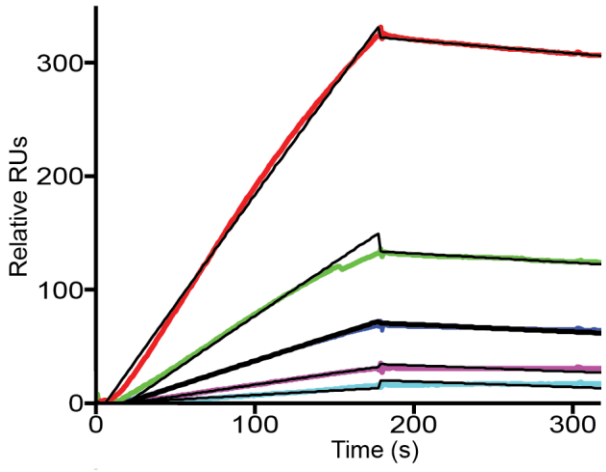
Relative RUs
300
200
100
0
0
100
200
300
Time (s)

Supplementary Figure S6. SPR analysis of PRDC binding to immobilized heparin. SPR sensorgrams of PRDC-heparin interaction utilizing a heparin coupled sensor chip. Concentrations of PRDC (from top to bottom) were 20, 10, 5, 2.5 and 1.25 nM respectively.

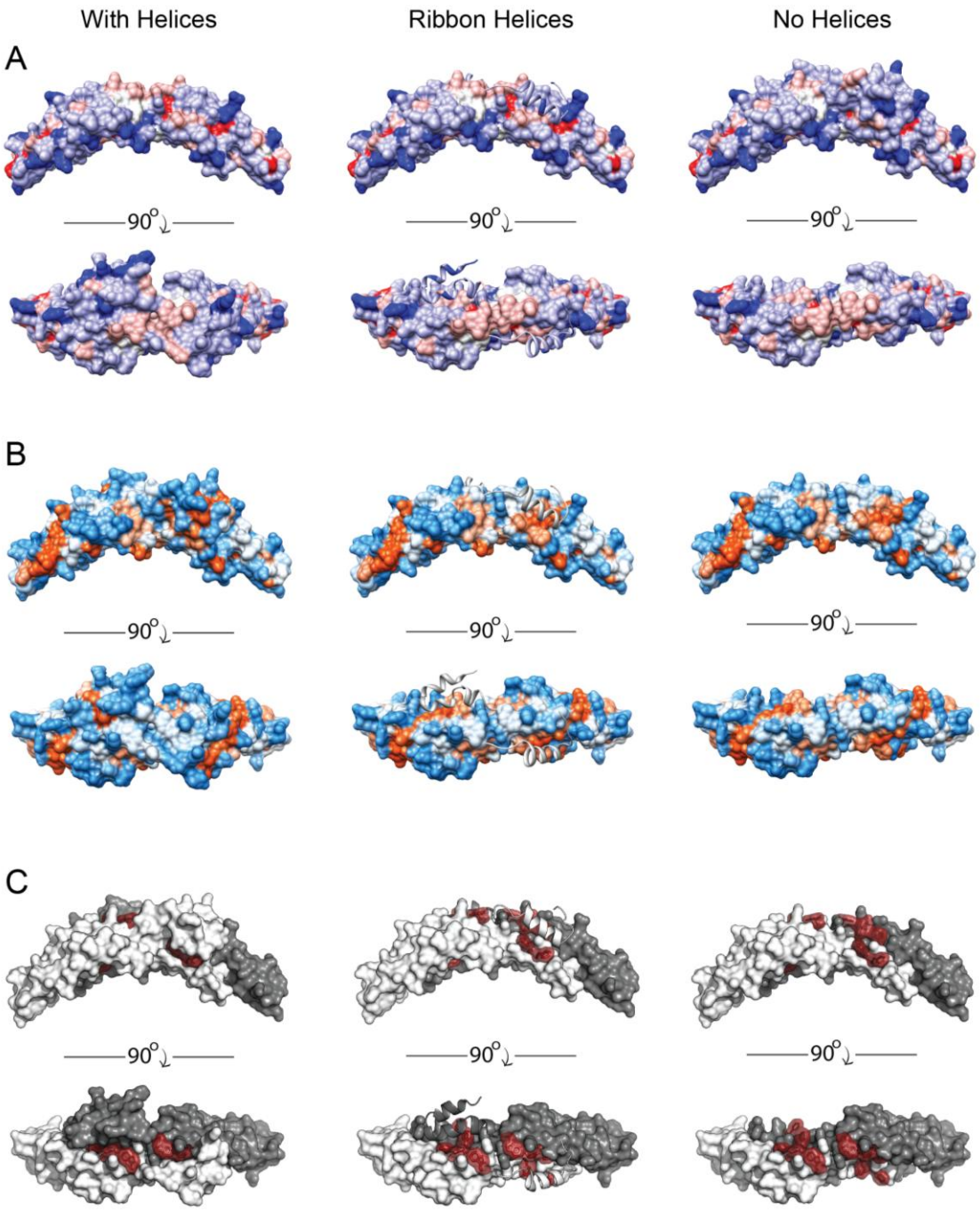
With Helices
Ribbon Helices
No Helices
A
90°
90°
90°
B
90°
90°
90°
C
90°
90°
90°

Supplementary Figure S7. DAN-family conservation and hydrophobicity mapped onto the structure of PRDC. (**A-C**) Surface structure of PRDC shown in both the top and side view either containing the N-terminal helicies, showing them in ribbon represention, or lacking them entirely. (A) Surface representation of PRDC was generated using Chimera and colored based upon the ClustalW multiple alignment algorithm. For the alignment, the mature sequences of mouse PRDC and the human forms of Gremlin, Dan, and Coco were used, which represent the strongly characterized DAN-family members exhibiting a robust BMP inhibitory phenotype. The PRDC surface is colored by using a gradient scale (blue-white-red) ranging from 0.25 (colored dark blue) to 1 (colored dark red) with median conservation (0.625) being colored white. Cysteine residues were colored white in order to enhance the results of the alignment. (B) Surface representation of PRDC colored using Chimera based upon the Kyte-Doolittle scale for hydrophobicity. Colors represent a gradient where dodger blue represents the most hydrophilic residues, white represents the median, and orange-red represents the most hydrophobic residues. (C) Surface representation of PRDC colored using Pymol where Chains A and B are colored white and grey and the residues identified by mutagenesis for defining the BMP binding epitope have been colored in red.

Supplementary Tables

Table S1. Calculated Solution Scattering Parameters.

Protein	Conc. (mg/ml)	I_0 (cm^{-1})	R_g (Å) Guinier	R_g (Å) Real Space	D_{max} (Å)	NSD[a]
PRDC	0.5	0.012 ± 0.001	27.01 ± 1.84	27.32 ± 1.10	94.55	0.92 ± 0.06
	1.0	0.025 ± 0.001	26.84 ± 1.00	27.43 ± 0.51	93.95	0.95 ± 0.06
	1.8	0.046 ± 0.001	27.99 ± 0.69	28.74 ± 0.34	97.97	1.04 ± 0.08
C120S	0.6	10.544 ± 0.080	27.41 ± 0.33	27.72 ± 0.20	93.89	1.09 ± 0.06
	1.2	20.004 ± 0.223	27.39 ± 0.22	27.75 ± 0.18	93.82	1.12 ± 0.05
FoXS	-	-	22.88 (24.69)[b]	-	~90.0*	-

[a]Normalized spatial discrepancy (NSD) calculated by Damsel/DAMAVER when performing *Ab Initio* modeling and averaging.

[b]Values obtained in FoXS analysis were determined by comparing PRDC at 1.0 mg/ml to the predicted scattering profile of Chain B (or Dimer AB) in the PRDC crystal structure. D_{max} on the PRDC dimer was approximated using Pymol.

Supplementary Material and Methods

Small angle X-ray scattering analysis. For data reduction, averaging, transformation, and *Ab initio* model reconstruction, the software packages IGOR and ATSAS were used as previously reported (Deng et al., 2013; Ilavsky and Jemian, 2009; Konarev et al., 2003; Svergun, 1992; Svergun et al., 2001; Volkov and Svergun, 2003). Generated SAXS models were compared to the PRDC crystal structure using FoXS (Schneidman-Duhovny et al., 2010). For Guinier and Porod plot generation and analysis, the guidelines and methods for avoiding erroneous data analysis were used as described in a recently published manuscript by Rambo and Tainer (Rambo and Tainer, 2011; 2013). In brief, *I(0)* and R_g approximations were made such that data points were within acceptable parameters ($q \bullet R_g < 1.3$) within the linear portion of the low *q* data range. For Porod plot analysis, the points defining the linear range served as a starting point as higher *q* values were added back until a maximum value representing a plateau in either the $I(q) \bullet q^4$ versus q^4 or $I(q) \bullet q^3$ versus q^3 was reached (Rambo and Tainer, 2011). For the final represented *Ab initio* reconstructions, a minimum of 10 Gasbor ensembles was used to generate averaged models using DAMAVER (Svergun et al., 2001; Volkov and Svergun, 2003).

Heparin affinity measurements by Surface Plasmon Resonance. Biotinylated heparin was prepared by reacting sulfo-*N*-hydroxysuccinimide long-chain biotin (Piece, Rockford, IL) with free amino groups of unsubstituted glucosamine residues in the polysaccharide chain following a published procedure (Hernaiz et al., 2000). The biotinylated heparin was immobilized to streptavidin (SA) chip based on the manufacturer's protocol. The successful immobilization of heparin was confirmed by the observation of a ~250 resonance unit (RU) increase in the sensor chip. The control flow cell (FC1) was prepared by 1 min injection with saturated biotin. All experiments were performed and analyzed using a BIAcore 3000 system (Pharmacia Biosensor, Uppsala, Sweden) as previously described (Kattamuri et al., 2012). For equilibrium analysis, a constant amount of PRDC was pre-mixed with serial dilutions of free heparin, allowed to equilibrate for at least 15 min, and injected over the described BMP2 and BMP4 sensorchip. The flow rate was maintained at 20ul/min with a running buffer composition of 20mM HEPES pH 7.5,

150mM NaCl, 3.4mM EDTA, 0.005% polysorbate-20. The association phase was monitored using a dilution series of the described protein samples and observed for 10min. Following association, running buffer alone was applied over the sensorchip and the dissociation was monitored for 10min. Data were plotted for each sample using Scrubber 2.0, and then the amount of heparin required to inhibit 50% of binding to each flow cell was determined using GraphPad Prism (version 5).

Supplementary References

Deng, X., Morris, J., Chaton, C., Schroder, G.F., Davidson, W.S., and Thompson, T.B. (2013). Small-angle X-ray Scattering of Apolipoprotein A-IV Reveals the Importance of Its Termini for Structural Stability. Journal of Biological Chemistry *288*, 4854–4866.

Hernaiz, M., Liu, J., Rosenberg, R.D., and Linhardt, R.J. (2000). Enzymatic modification of heparan sulfate on a biochip promotes its interaction with antithrombin III. Biochem. Biophys. Res. Commun. *276*, 292–297.

Ilavsky, J., and Jemian, P.R. (2009). Irena: tool suite for modeling and analysis of small-angle scattering. Journal of Applied Crystallography *42*, 347–353.

Kattamuri, C., Luedeke, D.M., Nolan, K., Rankin, S.A., Greis, K.D., Zorn, A.M., and Thompson, T.B. (2012). Members of the DAN Family Are BMP Antagonists That Form Highly Stable Noncovalent Dimers. Journal of Molecular Biology *424*, 313–327.

Konarev, P.V., Volkov, V.V., Sokolova, A.V., Koch, M.H., and Svergun, D.I. (2003). PRIMUS: a Windows PC-based system for small-angle scattering data analysis. Journal of Applied Crystallography *36*, 1277–1282.

Rambo, R.P., and Tainer, J.A. (2011). Characterizing flexible and intrinsically unstructured biological macromolecules by SAS using the Porod-Debye law. Biopolymers *95*, 559–571.

Rambo, R.P., and Tainer, J.A. (2013). Super-Resolution in Solution X-Ray Scattering and Its Applications to Structural Systems Biology. Annu Rev Biophys, [Epub ahead of print].

Schneidman-Duhovny, D., Hammel, M., and Sali, A. (2010). FoXS: a web server for rapid computation and fitting of SAXS profiles. Nucleic Acids Res. *38*, W540–W544.

Svergun, D.I. (1992). Determination of the regularization parameter in indirect-transform methods using perceptual criteria. Journal of Applied Crystallography *25*, 495–503.

Svergun, D.I., Petoukhov, M.V., and Koch, M.H. (2001). Determination of domain structure of proteins from X-ray solution scattering. Biophys. J. *80*, 2946–2953.

Volkov, V.V., and Svergun, D.I. (2003). Uniqueness of ab initio shape determination in small-angle scattering. Journal of Applied Crystallography *36*, 860–864.